
Chapter IV

Modification of Chitosan-based Biodegradable Solid Polymer Electrolyte by Irradiation with MeV Ions

4.1 INTRODUCTION

4.2 RESULTS AND DISCUSSION

4.2.1 XRD Analysis

4.2.2 FTIR Analysis

4.2.3 Optical Analysis

4.2.4 AC Electrical Frequency Response

4.2.5 AFM Analysis

4.3 CONCLUSIONS

REFERENCES

Paper published in peer-reviewed journal related to this chapter:

1. Modification of chitosan-based biodegradable polymer by irradiation with MeV ions for electrolyte applications
Gnansagar B. Patel, N.L. Singh, F. Singh
Materials Science & Engineering B 225 (2017) 150–159
doi: [10.1016/j.mseb.2017.08.023](https://doi.org/10.1016/j.mseb.2017.08.023)

Chapter IV

Modification of Chitosan-based Biodegradable Solid Polymer Electrolyte by Irradiation with MeV Ions

4.1 Introduction

Chitosan has engrossed worldwide attention to achieve the desired functionalities owing to ease of processability and customization features. Indeed, $-\text{NH}_2$ and $-\text{OH}$ functional groups of chitosan made it assessable to the vast field with multidimensional functionalities and have an impressive mechanical strength, chemical resistance and thermal stability up to $200\text{ }^\circ\text{C}$ due to hydrophilicity nature in explicit forms such as gels, nanofibers, scaffolds, nanoparticles, films, etc. [1–3]. Particularly, acetate form of chitosan is preferred due to contributing ionic conductivity, better antibacterial activity, and efficient reduction ability of metal ions into metal nanoparticles [4]. The presence of a lone pair of electrons due to oxygen and nitrogen atoms of chitosan enable to form complexes with the salt. Hence, the second most abundant biopolymer chitosan, afterward the cellulose, is an excellent host matrix used as solid polymer electrolytes (SPEs). As, explained in Chapter 1 (section 1.4.2), soft, self-sustained, and flexible chitosan-based SPEs being used in the various applications of electrical and optical devices [1–5]. In SPE matrix, doped inorganic salts are dissociated in the polymeric matrix, which is responsible for the ionic conductivity. However, SPEs have room temperature ionic conductivity that is found inferior ranging between 10^{-8} to 10^{-7} S/cm hindered its implementations [5]. The SPEs may have crystalline and amorphous phases, but the conductivity is significant in the amorphous state. Generally, two distinct approaches being adopted to overcome the conductivity limitations. The incorporation of organic carbonate liquid plasticizers possesses lower molecular weight or ionic liquids into the chitosan host matrix. Although the improved conductivity is on the cost of mechanical and electrochemical degradation. Another promising one is to incorporate nanostructured additives such as TiO_2 , BaTiO_3 , SiO_2 as well as Ag, Cu Fe, and Au nanoparticles. The perspective behind such an approach is to reduce the crystalline structure of biopolymer-based SPEs. Both adopted

approaches being used to enhance the various dielectric features of the biopolymer could possible up to a certain extent, afterward, the matrices could not respond to additives. Hence, apart from tedious perspectives, the physical characteristics of the chitosan-based biodegradable SPE matrix will be further contrived by using a well-controlled SHIs irradiation technique. As discussed in Chapter 1 (section 1.4.2), in the present investigation on Eco-friendly SPE matrix, we have particularly preferred silver nitrate salt because of its inadequate studied with chitosan. The synthesis of flexible, soft, and self-standing SPE matrices doped with different wt% of AgNO_3 , the SHIs irradiation experimental details, and consequently characterization techniques have been described in section 2.2., 2.3, and 2.4 of Chapter 2, respectively.

4.2 Results and Discussion

4.2.1 XRD Analysis

To study the doping attributes of silver nitrate salt with chitosan (CS) polymer, the XRD spectra of pure chitosan and chitosan–silver nitrate salt complexes have been recorded at 2-theta angles of $5^\circ \leq 2\theta \leq 65^\circ$ and depicted in Figure 4.1. The diffraction peaks evolved at 8.2° , 11.6° , 15° , 18° , and 21.7° are identified as the characteristic peaks of pure chitosan as discussed in Chapter 3 (section 3.2.1). The XRD graphics revealed that upon doping of silver nitrate salt, the diffraction peaks correspond to chitosan have been suppressed and a reformed broad peak yielded. Indicating a substantial synergic dealing between the chitosan matrix and silver nitrate. The broadening of the peak indorsed to the augmented separation between confined polymeric chains of the SPE was introduced with salt. The thermal heating during the synthesis displayed the temperature of about $60 \pm 2^\circ\text{C}$ of SPE film-forming complex also assisted to achieve the amorphous phase. Although the diffraction peaks relevance to silver nitrate salt are not perceived in the XRD spectra. Implying the structural reformation of biodegradable host matrix and salt with no extant of surplus salt in the SPE, but the crystalline peaks evolved at 2-theta values of $\sim 38^\circ$ and $\sim 44^\circ$ resemble to the (1 1 1) and (2 0 0) planes of silver nanoparticles, respectively. Indeed, chitosan plays a versatile role as reducing and capping agents both in the

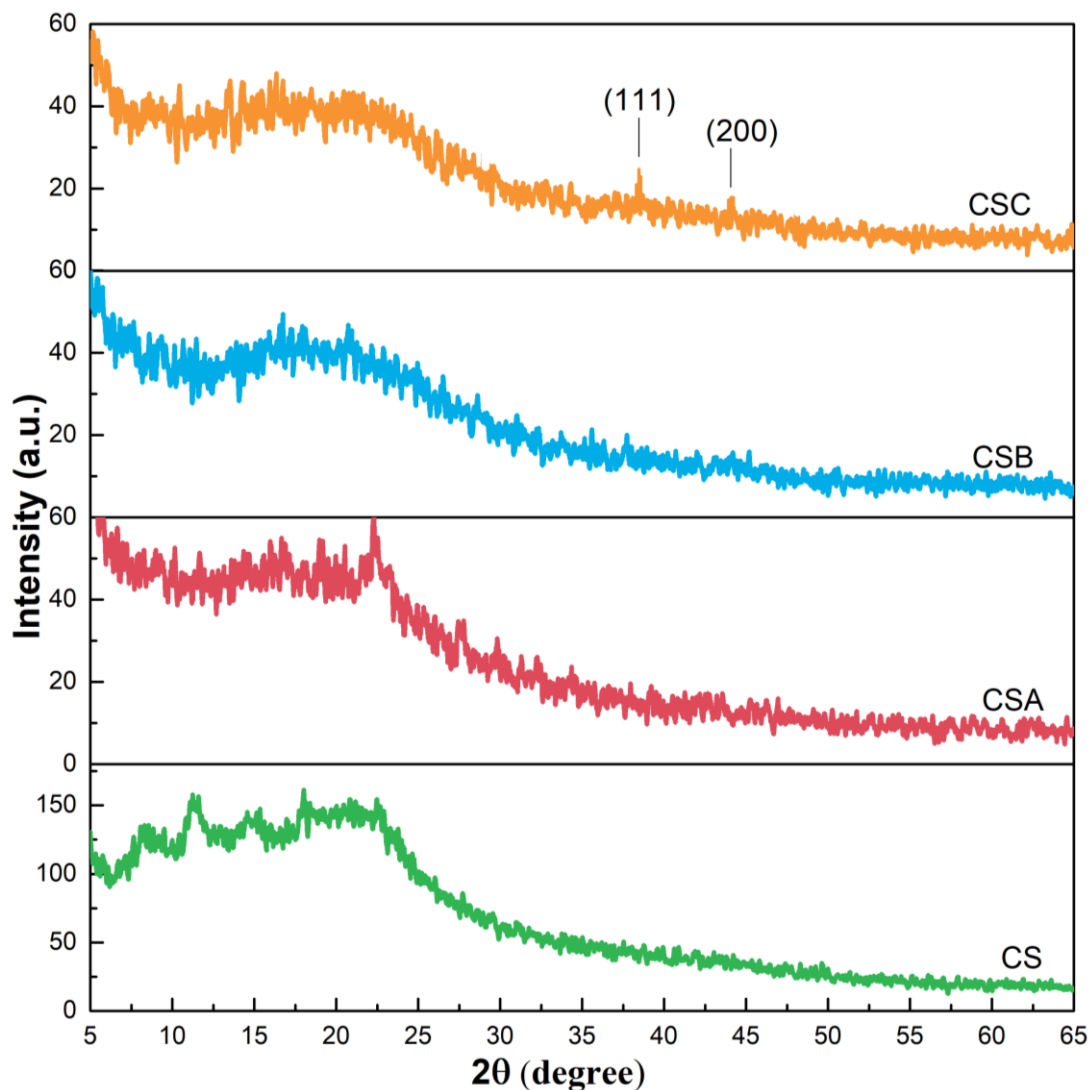


Figure 4.1 XRD patterns of CS and SPE system with different concentrations.

moderately heated film-forming complex yielding silver nanoparticles [6]. In addition, the XRD graphics of post C^{+5} and Ni^{+7} ions exposed SPE system did not display any remarkable change.

4.2.2 FTIR Analysis

As discussed in Chapter 2 (section 2.4.2), the IR spectra of SPE in transmittance mode have been recorded to avail the interaction of macromolecules with silver nitrate salt and SHIs impact on the functional groups/chemical linkages within SPE matrices. Figure 4.2 represents the IR spectra of CS and highest conducting electrolyte system CSC. There is a deficiency of peak at 1590 cm^{-1} corresponds to $-\text{NH}_2$, but the peak evolved at 1540 cm^{-1} is evidence of NH_3^+ vibrational mode. This resembles the acetate form of biodegradable SPE matrices [4]. In

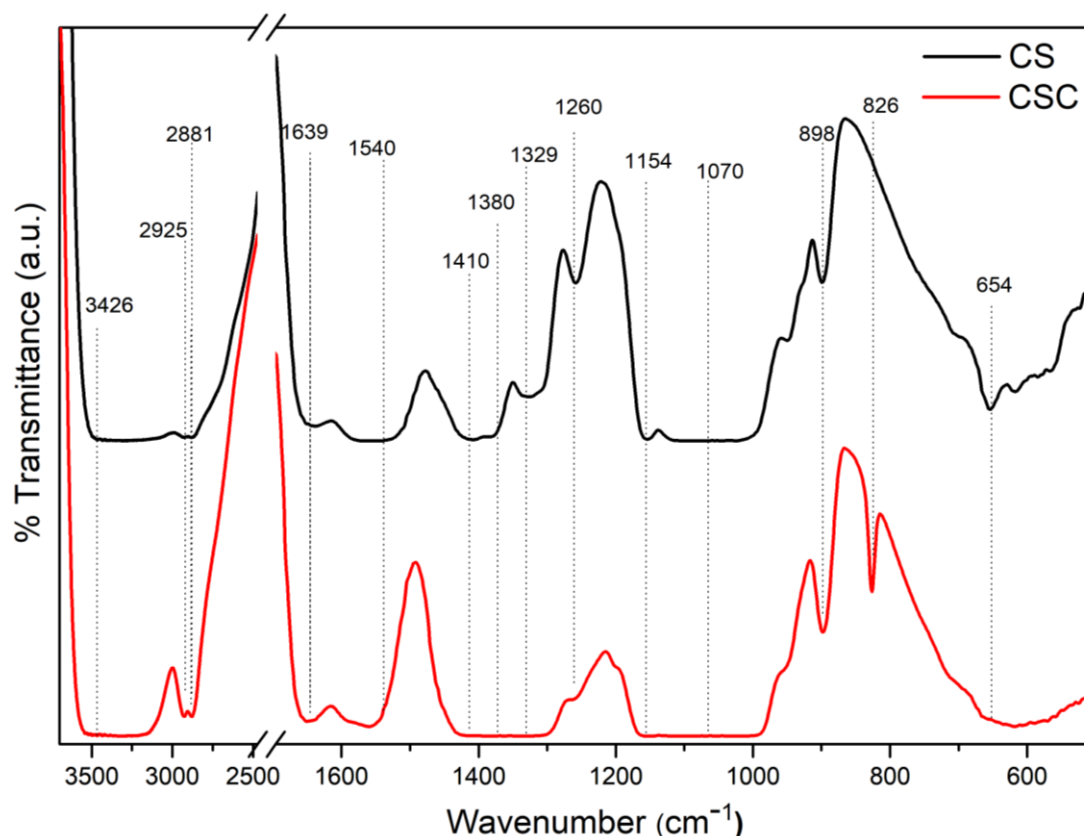


Figure 4.2 FTIR spectrum of CS and CSC SPE samples.

addition, as seen from [Figure 4.2](#), the formation of a newer vibrational band at 826 cm^{-1} allocated to residual NO_3^- from silver nitrate salt within SPE matrices [7]. While the persisting vibration modes as seen in [Figure 4.2](#) are assigned to the characteristics groups and linkages of chitosan as explained in Chapter 3 (section 3.2.2).

The concentration-dependent IR spectra of chitosan-based biodegradable SPE matrices revealed in [Figure 4.3](#). It is observed from [Figure 4.2](#) and [Figure 4.3](#) that the addition of salt in electrolyte matrices yielded a shift in absorption peaks of CS positioned at 898, 1154, 1329, 1410, 1540, and 1639 cm^{-1} to 897, 1143, 1324, 1404, 1559 and 1650 cm^{-1} , respectively. Moreover, it seems that the intensities of peaks appeared at 898, 1540, 2881, and 2925 cm^{-1} increased, whereas intensities of other peaks in IR spectra resembling distinct vibrational modes exhibited a decreasing tendency. Also, perceived peak broadening might validate the enhanced concentration of free ions. The peaks existed at 1380 and 665 cm^{-1} wavenumbers are completely suppressed. However, the deficiency of vibrational modes in IR spectra relevant to silver nitrate at 1800, and 1430 cm^{-1} are absent, implying proficient salt–matrix complexation [8]. The mode at 826 cm^{-1} is allocated to the O-N stretching vibration of the nitrate group.

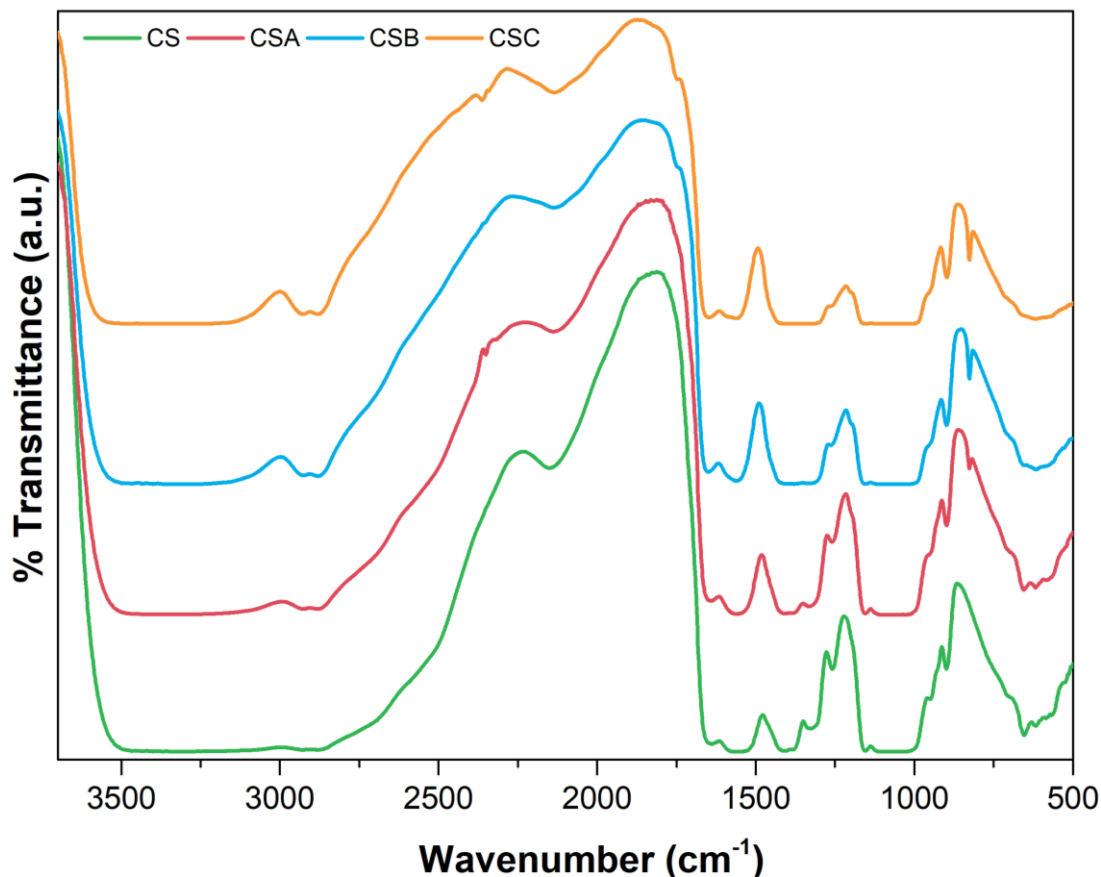


Figure 4.3 The concentration-dependent FTIR of chitosan-based SPE system.

These analyses infer that there is a significant interaction of the metal ions or salt with chitosan, which plays an important role in the ionic conductivity of SPE.

Figure 4.4 displays the FTIR graphics of pre and post C^{+5} and Ni^{+7} ions irradiated CSC SPE matrix at different fluences. As a consequence of SHIs irradiation of SPE matrix, comprehensive waning in the transmission intensity of all the peaks without any considerable change in the peak position. The contraction in intensity indorsed to the transformation in localized chemical linkages of CSC through the abstraction of inter and intra-chain hydrogen bonds coupled with fundamental NH_2 and/or OH groups of chitosan macromolecule. As the SHIs moved through the biodegradable SPE matrix, triggered inter excitation and ionization of electrons within engendered transient molten zone along the ion trajectory. The electronic energy loss of C^{+5} and Ni^{+7} ions in chitosan is in the range of few keV/nm, as inferred in Chapter 2 (section 2.3.3). Because the strength of the chemical linkage in the polymer matrix is of the order of a few electron volts [10], there could be scission of all the bonds in the zone of the ion track, thereby leading to the formation of free radicals or ions due to the heterolysis

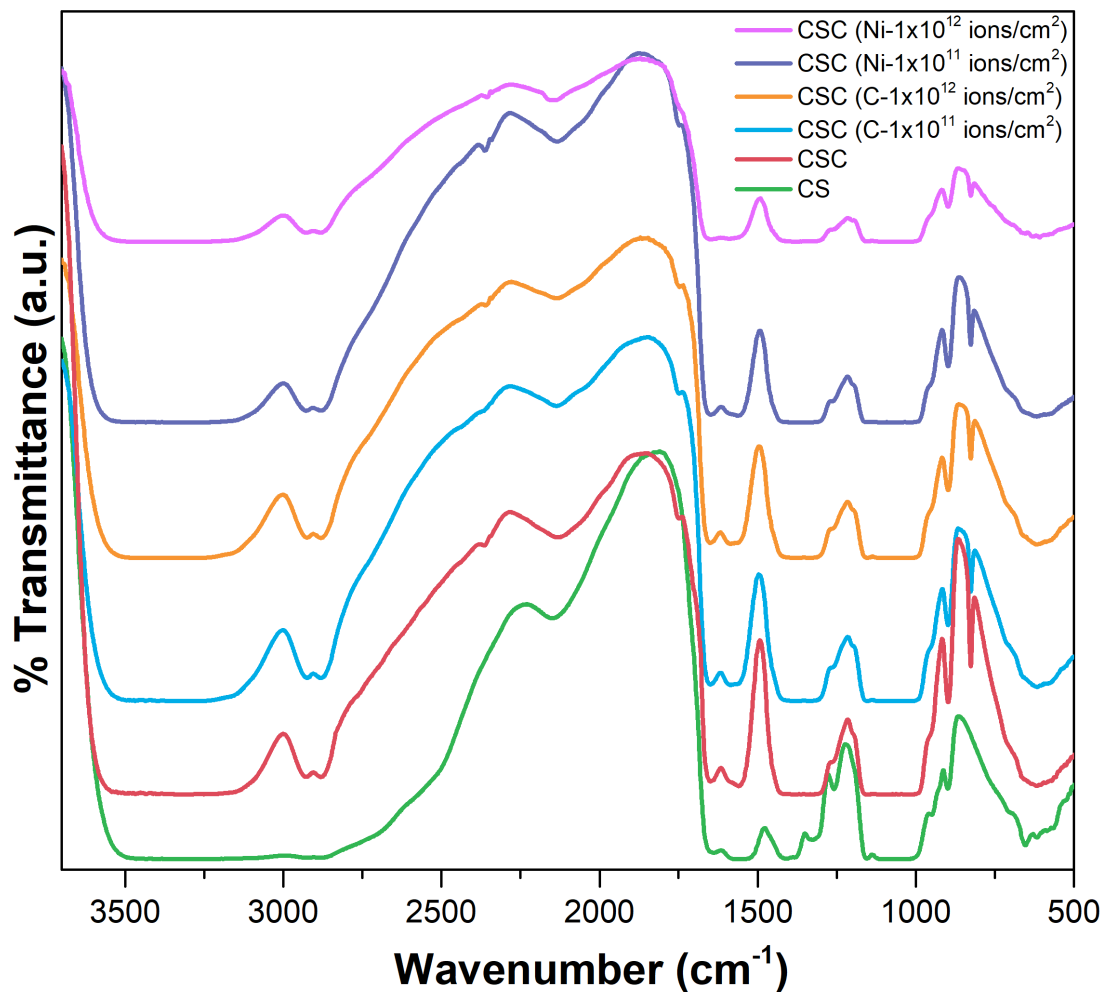


Figure 4.4 FTIR spectra of SPE samples irradiated with 60-MeV C^{+5} and 100-MeV Ni^{+7} ions at the fluences of 1×10^{11} and 1×10^{12} ions/cm², respectively.

or homolysis bond cleavages in the SPE system, respectively [11]. The fragmented species of lower molecular weight might residue eternally within the matrix or evacuate the host matrix due to a high vacuum shield. Because of multiple thermal quenching, the chemical configuration of the SPE matrix was reorganized through randomization and degradation of macromolecular chains. The macromolecular structural reform reasonably exhibited the fluence-dependent responses. In addition, the impact of heavier Ni^{+7} ions owing to tremendous S_e value imparted the remarkable amorphization than lighter C^{+5} ions.

4.2.3 Optical Analysis

The optical studies of biodegradable SPE matrices by concern doping level and ions irradiation fluence have been investigated using the UV–Vis absorption spectroscopy. The absorption

spectra are explicitly used in the analysis of optical bandgap and also to determine the kind of electron excitation. The absorption peak evolved at 310 nm can be accredited to the transformation of glucosamine into glucosamine acetate as clearly seen in Figure 4.5. This is a strong consolation with IR response, which shows the acetate form of biodegradable SPE. The effect of silver nitrate salt concentration on the absorption of SPE films can be observed from Figure 4.5. Upon doping of salt, a well-resolved peak centred at 428 nm as compared to CS is evidence of the surface plasmon resonance (SPR) of Ag nanoparticles [12,13]. Due to the increased doping concentration of silver nitrate, the intensity of the peaks seems to be increased because of the glucosamine acetate nature of the matrix and the presence of Ag nanoparticles. This can be attributed to effectual chemical interaction between chitosan and AgNO_3 as well as enhance in Ag nanoparticles concentration within the matrix, respectively. After SHIs irradiation, the intensity of the SPR peak increased, which is relevant to Ag nanoparticles, as displayed in Figure 4.6. Indeed, the availability of an abundant number of free electrons during the SHIs irradiation enables the transformation of Ag^+ ions into metallic Ag^0 nanoparticles *via* static charge transfer process [14]. Moreover, the redshift in the absorption edge (AE) is perceived on account of $\pi \rightarrow \pi^*$ electronic transition [15]. This kind of transition triggers in the unsaturated centers and also indicated that the materials possess double or triple bonds [15].

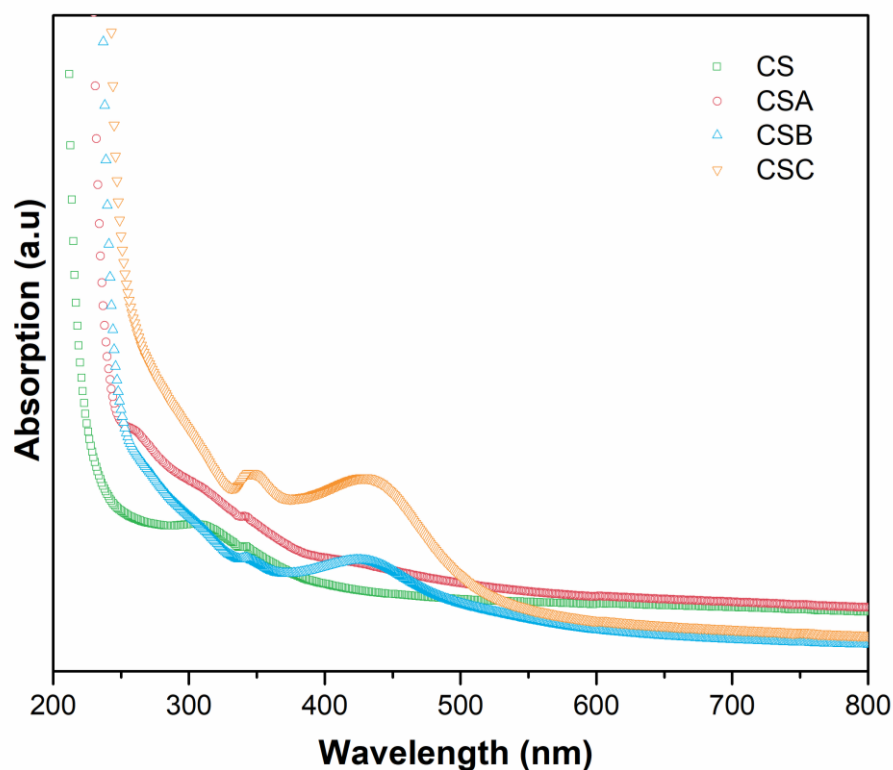


Figure 4.5 UV–Vis spectra of concentration-dependent SPE samples.

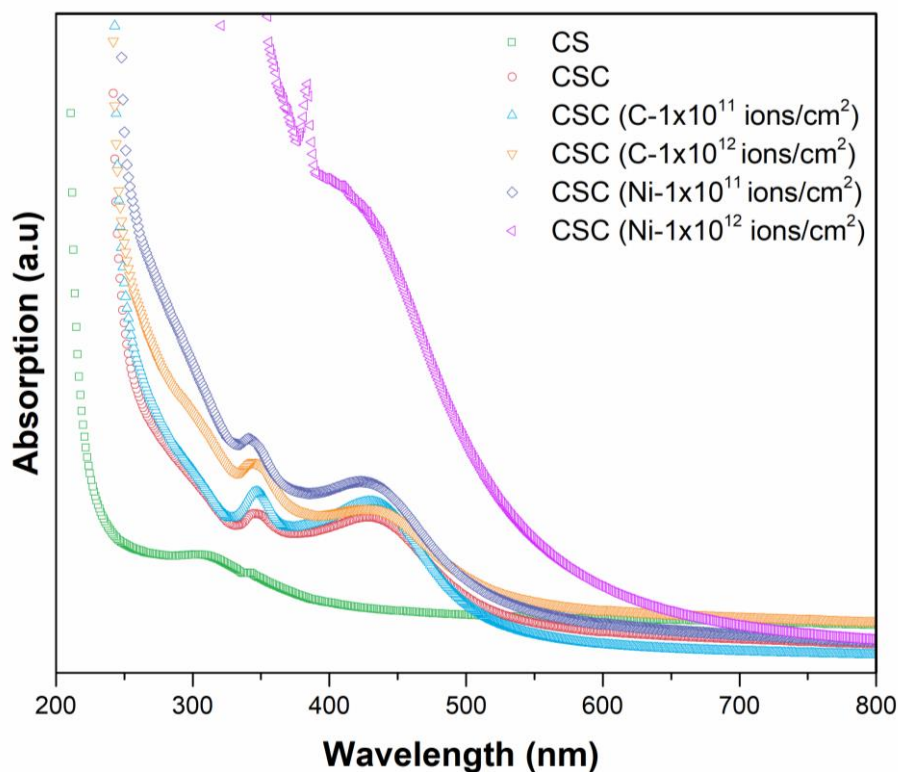


Figure 4.6 UV–Vis spectrum of CS and CSC samples irradiated with 60-MeV C^{+5} and 100-MeV Ni^{+7} ions at the fluences of 1×10^{11} and 1×10^{12} ions/cm², respectively.

Conclusively, the doping instigates the persuasive compatibility and interactions between the NH_2 and/or OH functional groups chitosan and silver ions. This can be signified and perceived in the change in crystallinity and vibrational modes of the SPE system as explained in their XRD and FTIR responses, which could affect the bandgap. As a consequence of C^{+5} and Ni^{+7} ions irradiations, the AE of the absorption spectra eventually became broader and successively move toward the visible regime, and the extent of Ag nanoparticles rises. The reformed AE exhibits the fluence-dependant responses ascribed to the defects formation along with the fragmentation of various low molecular-weight radicals and ions. These transformations might facilitate the excitation of non-bonding electrons from the valance band to the conduction band [16]. This confirms a waning in optical bandgap because of SHI irradiation, which functionalized the dielectric attributes of the SPE.

As explained in Chapter 2 (section 2.4.3), Tauc's method and linear least-squares statistics were employed to avail a kind of transition between the parabolic bands and the optical bandgap [17]. The Tauc plot of SPE matrices shows a reliable fitting for $n = 0.5$, which confirms the direct allowed transition. The fluence-dependent variation in optical

Table 4.1 Variation in optical energy bandgap (E_g) and the number of carbon atoms per conjugation length (N) at different fluences of 60-MeV C^{+5} and 100-MeV Ni^{+7} ion irradiation for SPE samples.

Sample	Carbon (60 MeV)		Nickel (100 MeV)	
	E_g (eV)	N	E_g (eV)	N
Pristine CS	5.64 ± 0.02	37	5.64 ± 0.02	37
Pristine CSA	5.20 ± 0.02	44	5.20 ± 0.02	44
CSA (1×10^{11} ions/cm ²)	5.01 ± 0.02	47	4.66 ± 0.03	54
CSA (1×10^{12} ions/cm ²)	3.96 ± 0.01	75	3.07 ± 0.01	125
Pristine CSB	4.87 ± 0.02	50	4.87 ± 0.02	50
CSB (1×10^{11} ions/cm ²)	4.81 ± 0.02	51	4.45 ± 0.03	59
CSB (1×10^{12} ions/cm ²)	4.19 ± 0.01	67	2.92 ± 0.04	138
Pristine CSC	4.62 ± 0.02	55	4.62 ± 0.02	55
CSC (1×10^{11} ions/cm ²)	3.56 ± 0.00	93	3.42 ± 0.01	100
CSC (1×10^{12} ions/cm ²)	3.47 ± 0.01	98	2.89 ± 0.01	141

energy bandgap of SPE matrices is listed in Table 4.1. Upon C^{+5} and Ni^{+7} ions irradiations, an attenuation in values of E_g was perceived for all the biodegradable SPE matrices. The attenuation in E_g might be induced to the formation of an intermediate sub-band state due to energetic ions impact. The value of E_g due to silver nitrate doping reduced to 4.6 eV (CSC) from 5.6 eV (CS), whereas, the corresponding values upon C-ion and Ni-ion decline to 3.5 and 2.9 eV, respectively. Hence, SHIs irradiations tremendously affect the bandgap of the CSC matrix by $\sim 24.9\%$ and $\sim 37.4\%$ fall off, respectively. In addition, relatively superior S_e value of Ni-ions than the C-ions plays a crucial and essential role in a persuasive decrease in E_g . Indeed, heavier and energetic Ni-ion capably cause major defects at the edge of the conduction band that might be prolonged into the forbidden gap. Moreover, the degree of structural disorder or amorphization and enhanced density of fragmented species due to the heavier Ni-ions found to be substantial than the C-ions. The studies on polymeric system by the density of state implied that the level of polymer disorder shows their relevance in enhanced conductivity as well as waning in bandgap as an effect of MeV ions exposure [18,19]. As revealed from the IR responses of C^{+5} and Ni^{+7} ions irradiated SPE matrices, the vibrational mode assigned to the C–H linkages was considerably suppressed, which indicates the degassing of H_2 gas and some volatile gaseous products. Moreover, the characteristic optical signature of polymeric materials in general, can be represented by the H-concentration and the relevant studies carried out in the literature [20]. The H/C atomic fraction was found to be reduced on account of immense hydrogen elimination owing to microscopic structural degradation upon SHIs irradiation [20],

as previously mentioned in the FTIR section. Consequently, the biodegradable matrix possesses an exceed the extent of C atoms than the H atoms enable to form the carbonaceous clustering in the SPE matrix [15,16,18,20,21].

As mentioned in Chapter 2 (section 2.4.3), the modified Fink approach was used to estimate the consisting carbon atoms per conjugation length (N) of carbonaceous cluster [21]. The estimation of N for pre and post irradiated SPE samples are tabulated in Table 4.1. Convincingly, the boost in N values clearly indicates fluence and electronic energy loss dependent proceedings. Indeed, an abundant energy deposited per event and an increase in ion fluence instigated the multiple thermal quenching cascades in the grain structures of SPE [22]. The compact carbon clustering phenomenon is accredited to the reformation of the polymeric grain structure together with the degassing of volatile fragments and species [21,22]. The size of carbonaceous clusters play a crucial role in the electric characteristics of the SHI exposed SPE system.

4.2.4 AC Electrical Frequency Response

As mentioned in Chapter 2 (section 2.4.4), the dielectric spectroscopy of polymeric materials is a prosperous and perspective approach to unfold the electrical signatures and to elucidate the conductivity mechanism and molecular relaxation behavior. The Z-View2 software was used to procure the necessary data to express the dielectric response in distinct formalism.

The spectra of $\epsilon'(\omega) \rightarrow \log f$ for pristine and irradiated (C^{+5} and Ni^{+7} ions) SPE samples are displayed in Figure 4.7. The $\epsilon'(\omega)$ spectra indicate an enhanced response due to an assured effect on the dipoles concerning the silver nitrate salt concentration and ion fluence. The graphics of $\epsilon'(\omega)$ revealed a consonant increasing trend over a broader span of frequencies marks the onset of deformation, degree of polarization, and localized macromolecular movement under the action of the oscillating field. Indeed, charge drift, interfacial, and orientational polarization govern the frequency-dependent response of $\epsilon'(\omega)$. At the highest fluence and the lower frequencies (<10 kHz), the $\epsilon'(\omega)$ values remarkably increased and attained almost constant values at higher frequencies. In fact, at a lower frequencies regime, the reversing field varied relatively at a slower rate, so the charge carriers possesses a long-range drift. As a result, the level of carrier accumulation grows at the vicinity of the amorphous electrolyte/crystalline electrode surfaces, that is, the occurrence of interfacial polarization in

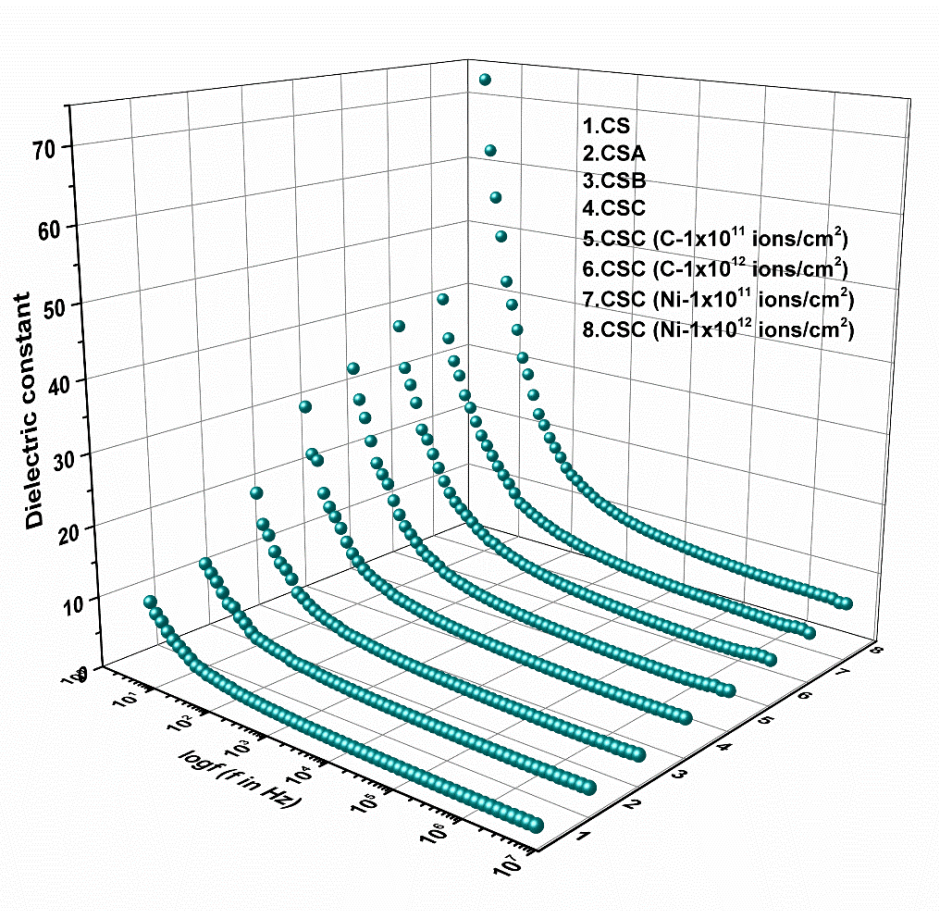


Figure 4.7 Plot of dielectric constant versus log frequency for pristine and irradiated SPE with 60-MeV C^{+5} and 100-MeV Ni^{+7} ions at the fluences of 1×10^{11} and 1×10^{12} ions/cm², respectively.

SPE [2,5,12,13]. The spectra of $\epsilon'(\omega)$ revealed that beyond the frequency of 10 kHz the dipoles instigated to lagging behind the time-varying field and adequately orientational polarization cease might probably decreased the values of $\epsilon'(\omega)$. While in the regime of higher frequencies, the dielectric constant procured a constant value because the dipoles no longer exhibited the pursuing response to the reversing field. Another assuring attribute to the observed decreasing response at high frequencies window is hindered charge carriers migration/drift through the dielectric medium and thereby the instigation of charge carriers neutralization cascades at defect sites by trapping [23]. Also, the polarization of trapped and bound charges cannot occur at higher frequency regions, thus decreasing the value of $\epsilon'(\omega)$ [24]. The increase in $\epsilon'(\omega)$ upon C^{+5} and Ni^{+7} ions irradiation clarifies the SHI-induced physicochemical reforms, explicitly, macromolecular structural degradation due to breaking numerous bonds and reduction of Ag^+ to Ag^0 as mentioned in IR and optical sections, respectively. The SHI-induced degradation facilitates the localized mobility of polymeric chain ascribed to the formation of low-

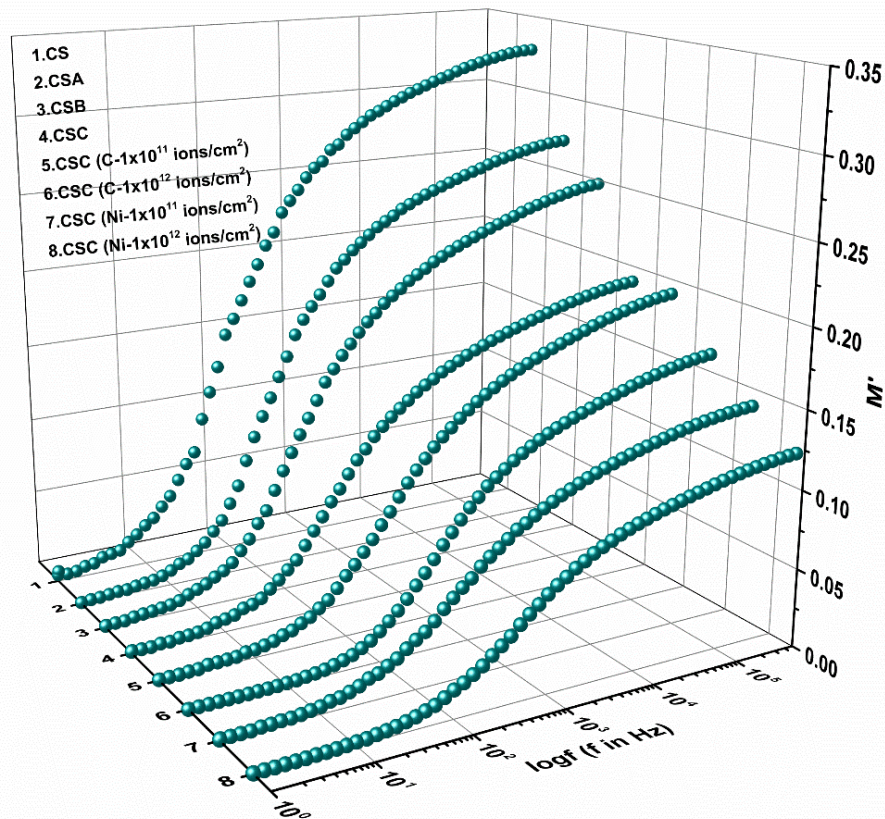


Figure 4.8 Plot of real part of modulus versus log frequency for pristine and irradiated SPE with 60-MeV C⁺⁵ and 100-MeV Ni⁺⁷ ions at the fluences of 1×10^{11} and 1×10^{12} ions/cm², respectively.

molecular-weight segments. The Ni⁺⁷ with superior electronic energy loss deposited the massive energy to the SPE system caused greater degree of degradation and thus enhanced the $\varepsilon'(\omega)$ more effectively.

The prospect of electric modulus formalism is an ingenious tactic of revelation used to unfold the sorts of relaxation and conduction phenomena in the biodegradable SPE system by suppressing the electrode polarization attributes. The complex electric modulus (M^*) with real (M') and imaginary (M'') electric modulus can be obtained using the complex permittivity as discussed in Chapter 2 (section 2.4.4) [25]. In the SPE system, the different relaxation process due to ion conductivity is suppressed in the real dielectric formalism. As the ions transported from one to another site might perturb the surrounding electric potential in the SPE system. As a result, the movement of the other ions within the nearby province of the perturbed potential is sensibly affected. Such an interactive transportation of ions leads to a conduction process or a nonexponential decay with a distribution of relaxation time [26]. The long-range conduction process and localized dielectric relaxation might explicitly explored by integrating complex

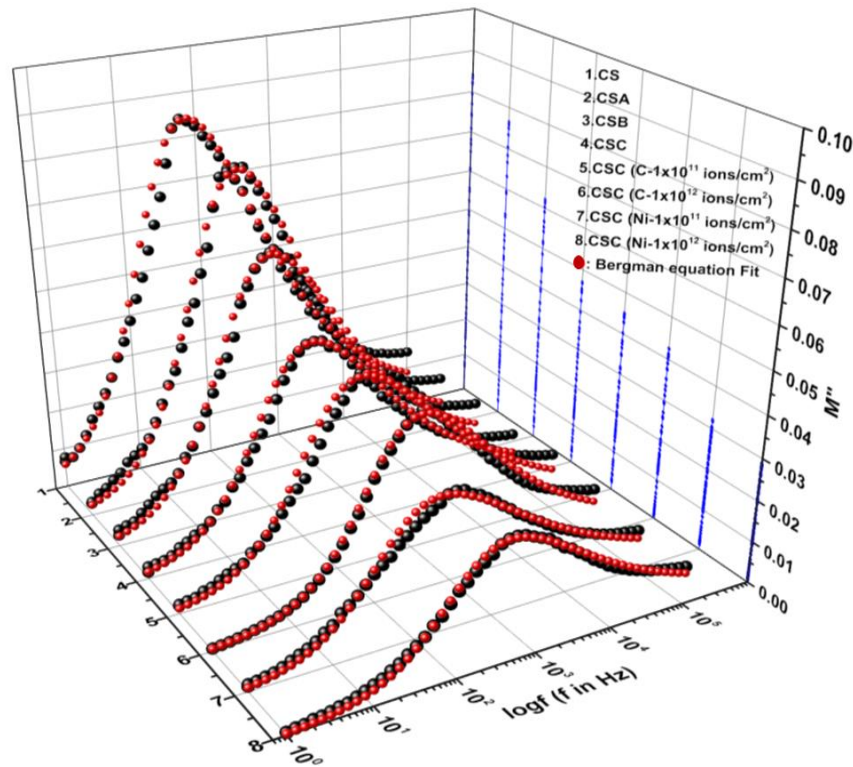


Figure 4.9 Bergman equation fit of imaginary part of modulus versus log frequency for pristine and irradiated SPE with 60-MeV C^{+5} and 100-MeV Ni^{+7} ions at the fluences of 1×10^{11} and 1×10^{12} ions/cm², respectively.

modulus and permittivity data. The spectra of $M'(\omega) \rightarrow \log f$ and $M''(\omega) \rightarrow \log f$ for pre and post SHIs exposed SPE samples in window of 1–100 kHz frequency at ambient temperature are depicted in Figure 4.8 and Figure 4.9, respectively. At first sight, the $M'(\omega)$ spectra at the lower frequencies approaching zero for pristine as well as MeV ions irradiated samples indorsed to the ionic conduction/removal of the electrode polarization effect at the low-frequency dispersion [25,26]. The $M'(\omega)$ graphics revealed the spreading across the broader span of frequencies and saturated (M_∞) at the higher frequencies. This indicates that the $M''(\omega) \rightarrow \log f$ spectra mark the onset of the characteristic relaxation phenomenon involving a well-resolved loss peak. The deficiency of peak in $M'(\omega) \rightarrow \log f$ graphics clearly point out the consonant analogy between the real part of $M^*(\omega)$ and the real part of $\epsilon^*(\omega)$. The concentration and fluence dependent overall decreasing responses of $M'(\omega)$ are perceived. Moreover, a dominant decline depicted for Ni^{+7} ions irradiation. This finding reveals that the local polymeric segmental motion improved along with enhance in charge carrier mobility [13,25,26], as a consequence of branching of polymer chains, as discussed in the FTIR section. The SHIs induced decrease in the real part of electric modulus is reassembly predicted from the enhanced dielectric constant of SPE matrices.

Table 4.2 Parameter values obtained from the Bergman equation fit and σ_{dc}

Sample	M_{max}''	f_{max}	β_{KWW}	FOM (%)	$\sigma_{dc} \times 10^{-7}$
Pristine CS	0.13200	179	0.42121	5.32	0.30 ± 0.06
Pristine CSA	0.11798	289	0.47594	7.17	0.61 ± 0.06
Pristine CSB	0.09673	311	0.42400	7.07	0.75 ± 0.03
Pristine CSC	0.07401	370	0.40418	6.69	1.12 ± 0.05
CSC (C- 1×10^{11} ions/cm ²)	0.07120	580	0.36286	6.94	2.02 ± 0.11
CSC (C- 1×10^{12} ions/cm ²)	0.06554	1000	0.40534	4.81	2.78 ± 0.13
CSC (Ni- 1×10^{11} ions/cm ²)	0.05102	590	0.34333	5.96	2.45 ± 0.13
CSC (Ni- 1×10^{12} ions/cm ²)	0.04533	1120	0.37309	5.31	3.46 ± 0.12

As illustrated in Figure 4.9, the $M''(\omega)$ spectra of all the SPE samples possess a well-resolved peak at an explicit relaxation frequency (f_{max}). The relaxation frequency inclusively inferred in terms of conductivity relaxation and transportation of charge carriers. The graphics reveal that the f_{max} monotonically shifted toward the regime of high frequencies window with a waning in the values of $M''(\omega)$ as a sign of doping of salt concentration and ions fluence of irradiation. These modifications upon SHIs irradiation were believed to respond in conductivity of SPE due to enhanced charge carrier density and formation conduction track. The low frequency relaxation ($f < f_{max}$) reveals a long-range diffusion of charge carriers and is attributed to the interfacial polarization. While high frequency ($f > f_{max}$) reveals a confined short-range movement of charge carriers and attributed to the segmental relaxation of polymeric chains in SPE.

As explained in Chapter 2 (section 2.4.4), the Kohlrausch–Williams–Watt (KWW) model [27] was amended by Bergman and a reliably preferable adoption for the fitting of graphics by adjusting the variables ϕ_{KWW} and β_{KWW} to comprehend the molecular dynamics and conductivity relaxation [28]. As depicted in Figure 4.9, the fitted spectra of $M''(\omega)$ resembled the red ball and the experimental one with the black ball. The graphic indicates a well-harmony between the theoretical estimation and experimental data. The reliability of Bergman fitting with procured experimental values of $M''(\omega)$ was monitored using the estimation of the figure of merit (FOM). The β_{KWW} , M''_{max} , and f_{max} parameters extracted from $M''(\omega)$ curve via the Bergman approach are summarized in Table 4.2 for each SPE sample. It is observed that the shape parameter β_{KWW} attained the values in between 0.34333 and 0.47594 indicate a non-

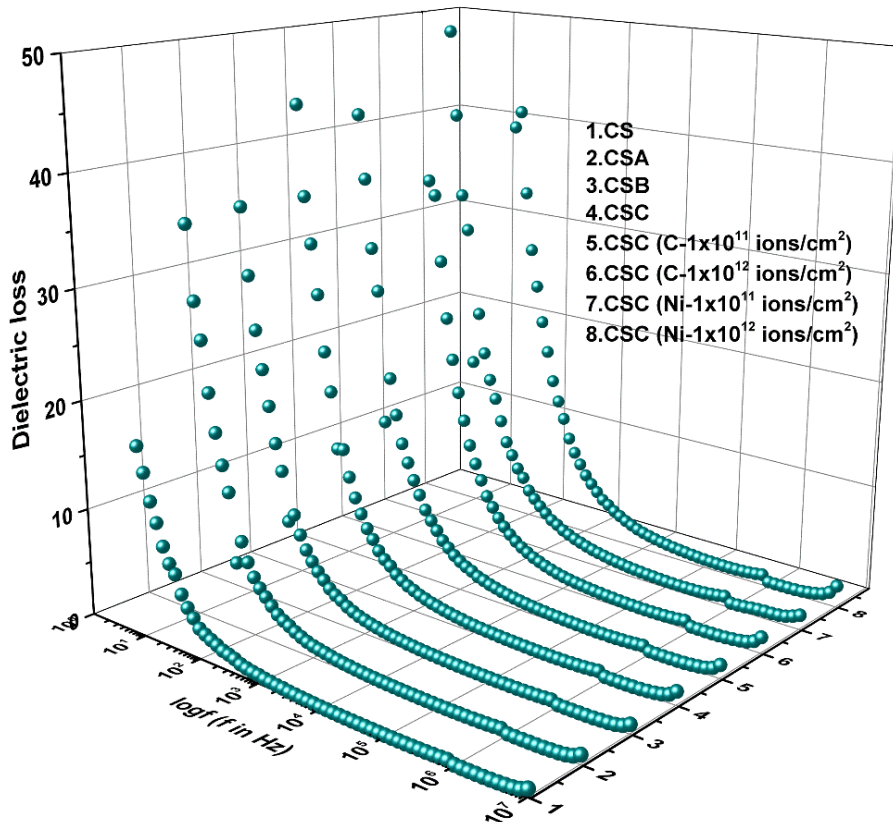


Figure 4.10 Plot of dielectric losses versus log frequency for pristine and irradiated SPE with 60-MeV C^{+5} and 100-MeV Ni^{+7} ions at the fluences of 1×10^{11} and 1×10^{12} ions/cm², respectively.

Debye type behavior of relaxation events occurred at the microscopic level. Moreover, the M''_{max} shows explicit dependency on the dopant concentration, ion species, and ion beam fluence and consequently shifted toward the high frequency side. These outcomes ultimately enhance the conductivity of biodegradable SPE due to improved charge carriers density and release of trapped charges. Relatively lowered values of shape parameter and the loss peak evolved in the spectra of $M''(\omega)$, whereas the peak deficiency in the spectra of $\varepsilon''(\omega)$ plot (See Figure 4.10) indicate that the events of a conduction process and the transport of ions and polymeric radicals are not isolated but both are potentially coupled. The modified response of frequency-dependent $M''(\omega)$ is due to structural degradation and defects formation upon MeV ions impact. The modulus response shows strong consonance with the significance of FTIR analysis.

Scaling of the $M''(\omega)$ spectrum is performed by implicating the extracted parameters *via* the Bergman model. As can be perceived from Figure 4.11 that the graphics of

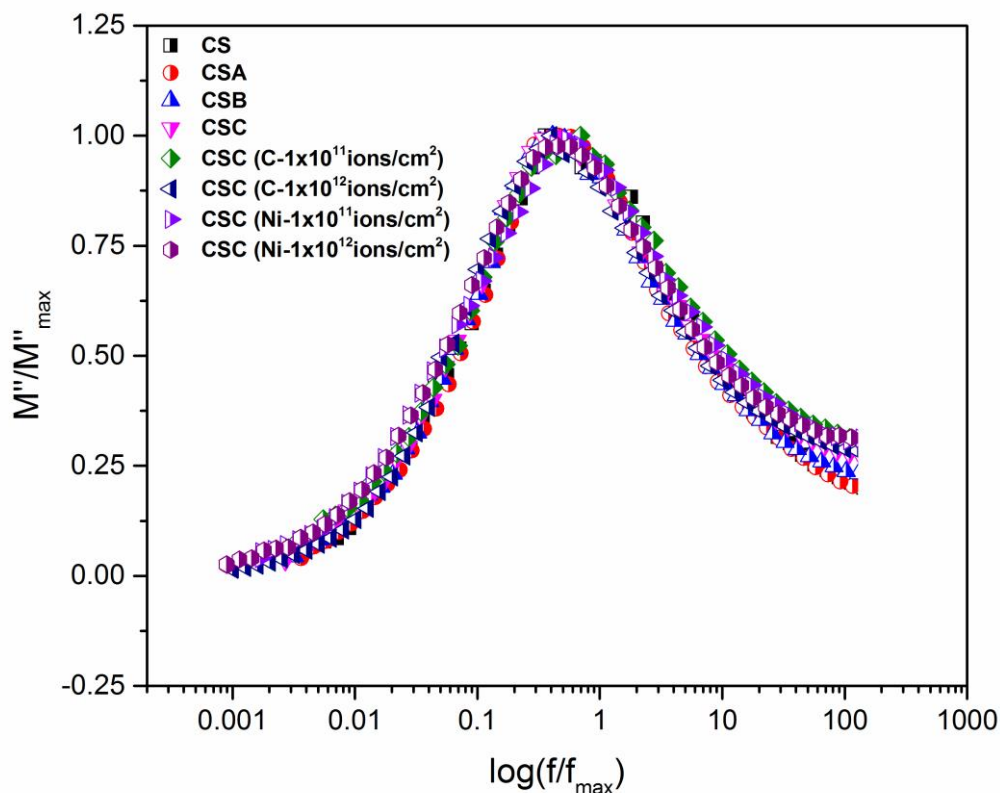


Figure 4.11 Scaling behavior of imaginary part of modulus for all the SPE samples.

$(M''/M''_{\max}) \rightarrow (f/f_{\max})$ for all the SPE films yielding a single master curve by adopting the maxima normalization method. This property suggests that the relaxation mechanism in the SPE matrix is not affected by dopant level or irradiation parameters.

The conductivity formalism of pristine and irradiated SPE samples can be conveyed as described in Chapter 2 (2.4.4). The graphics of $\sigma \rightarrow \log f$ illustrated in Figure 4.12 over a broad range of frequency for each SPE sample under investigation. The detectable plateau at the low frequency side endorsed to the long-range migration of charge carriers under the action of the reversing field. The values of σ_{dc} as a function of salt concentration and ion fluence with S.D. are listed in Table 4.2 and can be examined from Figure 4.13. As an increase in dopant level, the σ_{dc} increased from $\sim 3 \times 10^{-8}$ S/cm (CS) to 1.12×10^{-7} S/cm (CSC), whereas corresponding values increased to $\sim 2.78 \times 10^{-7}$ and $\sim 3.46 \times 10^{-7}$ S/cm due to C^{+5} and Ni^{+7} ions irradiation at a fluence of 1×10^{12} ions per cm^2 , respectively. As perceived in the finding of optical studies that the reduction phenomena of Ag^+ to Ag^0 explicitly fluence-dependant. The σ_{dc} for the SPE system is highly relevant to the presence of nanoparticle within the polymer matrix [29]. The

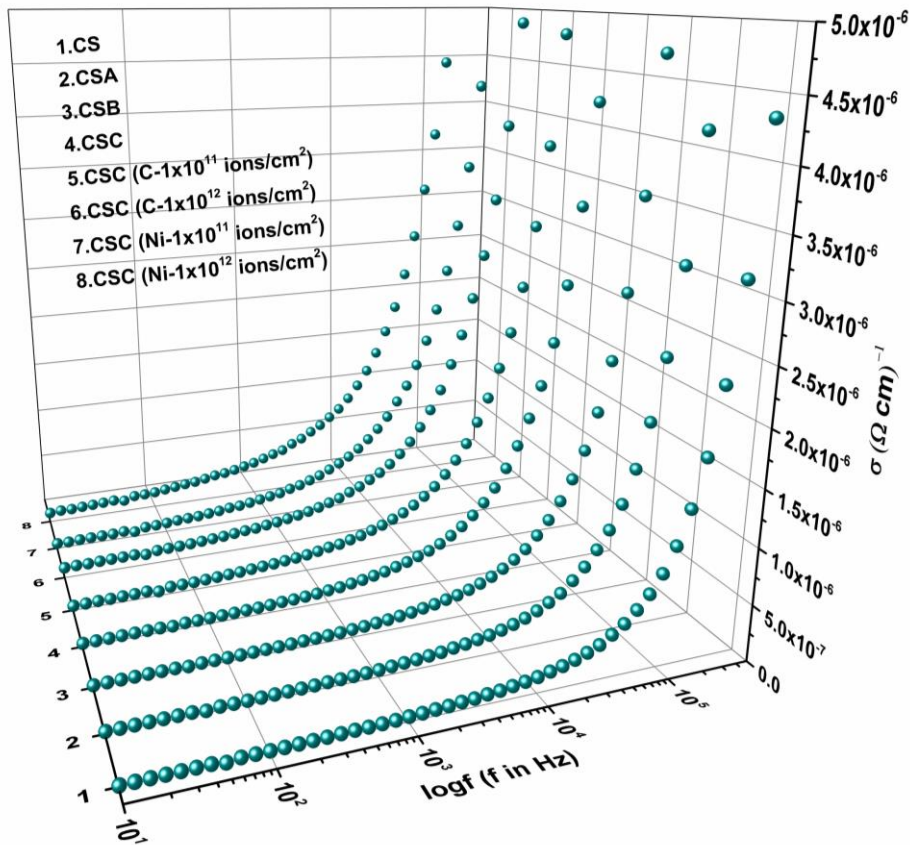


Figure 4.12 Plot of conductivity versus log frequency for pristine and irradiated SPE with 60-MeV C^{+5} and 100-MeV Ni^{+7} ions at the fluences of 1×10^{11} and 1×10^{12} ions/cm², respectively.

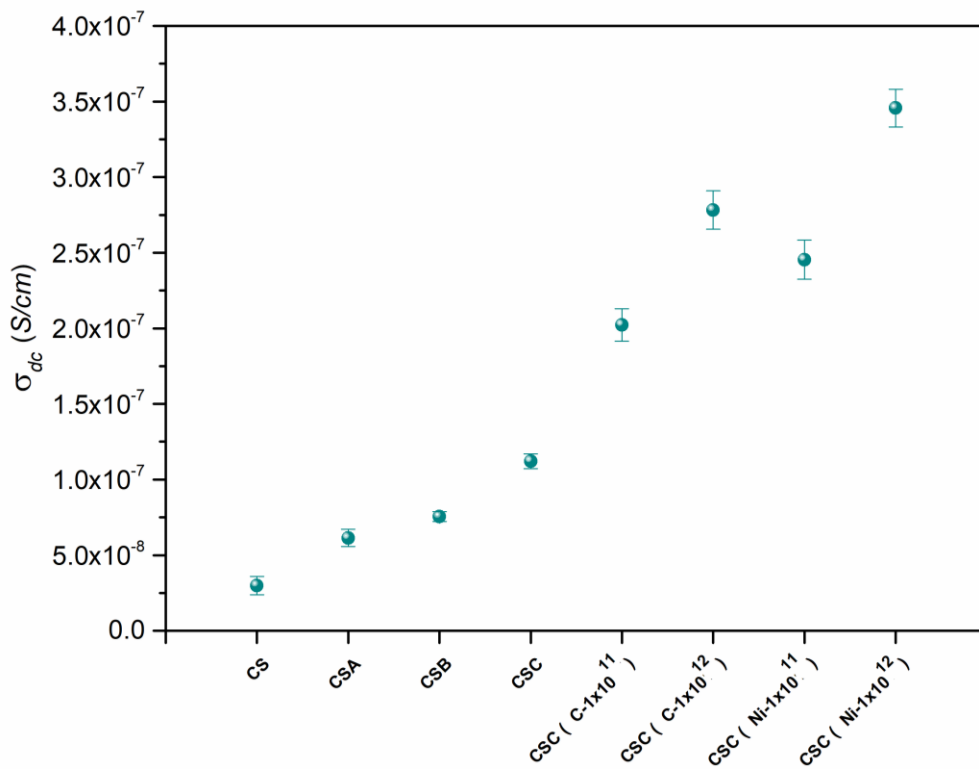


Figure 4.13 Variation in dc conductivity as a function of salt concentration and ion fluence.

effect of formed Ag^0 on σ_{dc} in the present investigation was recognized. Improved σ_{dc} conductivity suggests that disrupted crystallinity upon MeV ions irradiation might ease the transportation of charge carriers through the amorphous phase. A particular frequency at which the frequency independent plateau-like response turn into the frequency dependent dispersion response is referred to as the critical frequency (f_c). As the frequency changed to a higher scale from the lower one, the mean drift range of charge carriers waned and thus beyond f_c the conductivity pursues the power law $\sigma(\omega) \approx \omega^n$. This signature is attributed the disordered or inhomogeneous materials generally detected in broad dielectric spectroscopic investigations. After C^{+5} and Ni^{+7} exposor of SPE samples, the AC conductivity is encountered to be reasonably superior to the pristine one. The increase in conductivity can be ascribed to the increased free volume in the polymer matrix, scission of macromolecule chain, structural

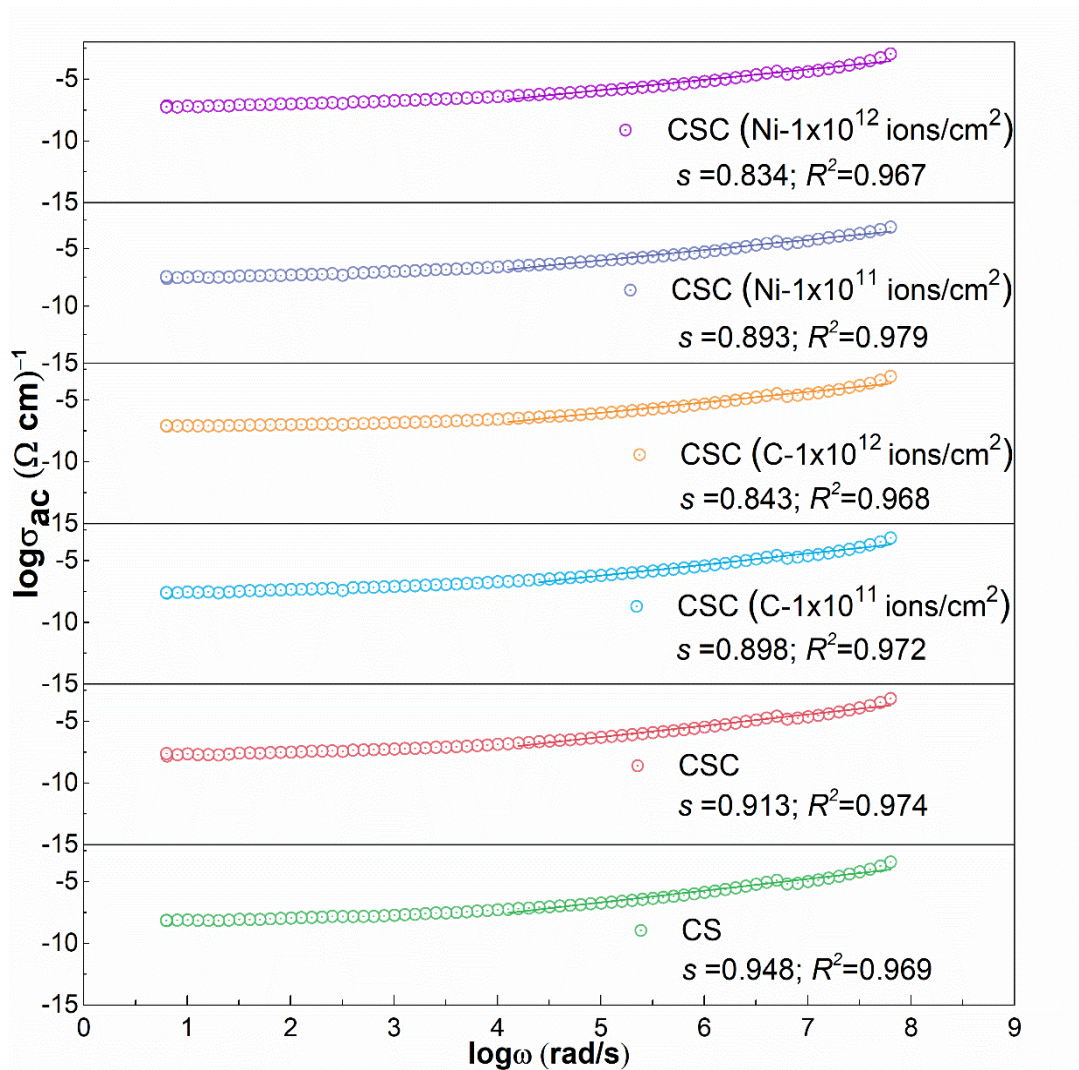


Figure 4.14 Plot of log ac conductivity versus log angular frequency for all the SPE samples.

degradation, creation of defects, and carbon-rich localized network [17,23,30,31]. In addition, the impact of Ni^{+7} ion irradiation on the frequency-dependent conductivity is significant and found to be fluence-dependent as well.

The hopping behavior of the charge carriers can be explained by the exponent s . As inferred in Chapter 2 (section 2.4.4), the exponent s can be calculated using the linear regression statistics performed to the slope ($d\sigma_{ac}/d\omega$) of $\log\sigma_{ac} \rightarrow \log\omega$ graphic in higher frequency region to eliminate the effect of space charge polarization. The obtained values of s are designated in the inset of the respective graph as can be seen in Figure 4.14. The measurement of s value is said to be

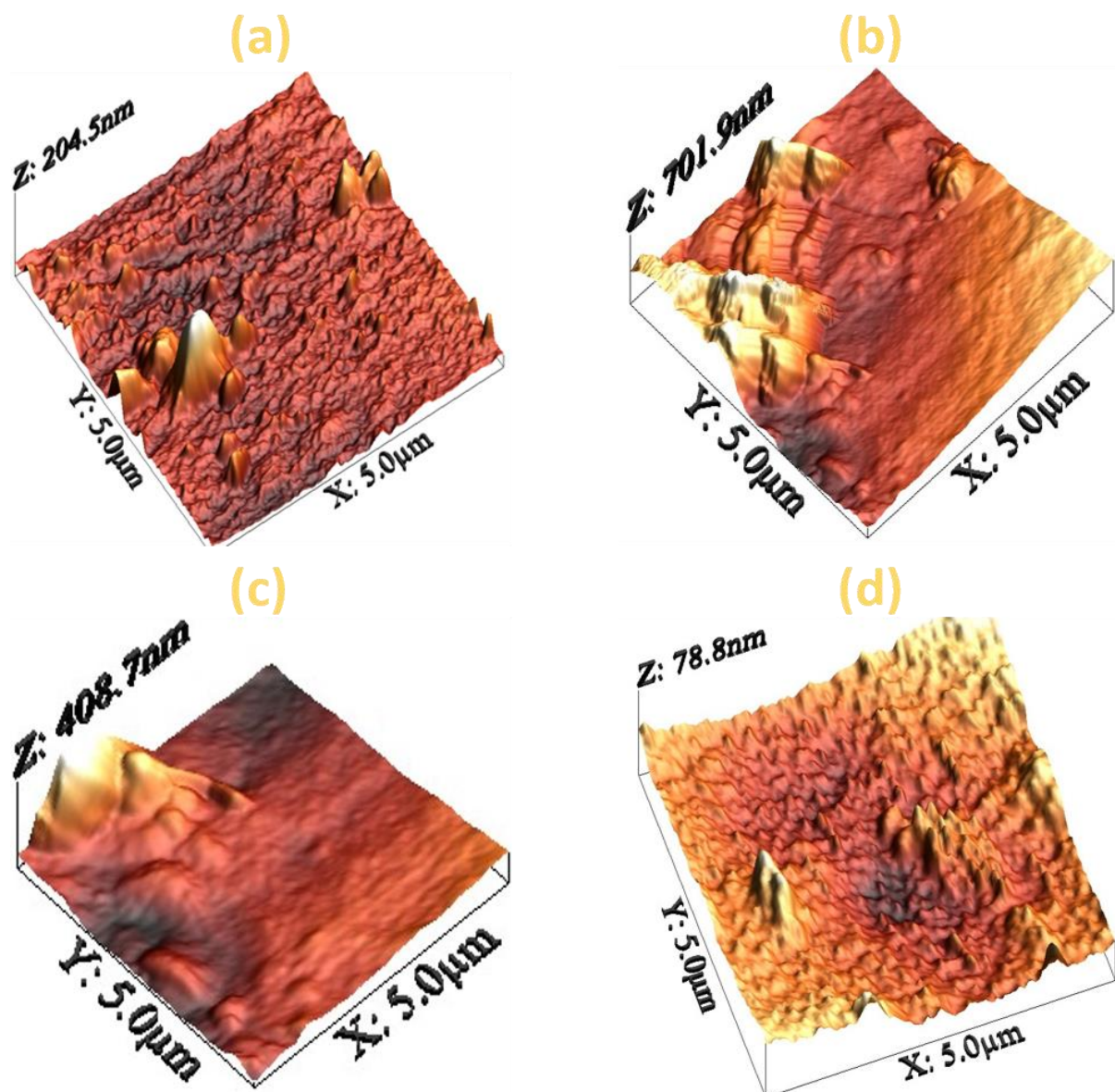


Figure 4.15 AFM images of CS (a) and CSC (b) films and CSC films irradiated with 60-MeV C^{+5} ions (c), 100-MeV Ni^{+7} ions (d) at the fluence of 1×10^{12} ions/ cm^2 .

precise with a reliable accuracy because the regression co-efficient R^2 found to be very close to unity. As examined that the values of s are ranging in between 0.98–0.83 with ± 0.02 S.D. Therefore, the conduction phenomenon in chitosan-based silver nitrate doped biodegradable SPE is due to the hopping of charge carriers, and it is AC type [24].

4.2.5 AFM Analysis

The three-dimensional AFM images to investigate the SHIs induced provokes on surface properties were performed over an area of $5 \times 5 \mu\text{m}^2$ for selected SPE samples as explained in Chapter 2 (section 2.4.5.2) and shown in Figure 4.15(a–d). The hillock-like structures (see Figure 4.15(a)) of different dimensions over the surface are perceived from the AFM image of CS AFM. Upon the inclusion of silver nitrate within the matrix, the average surface roughness (R_a) presumably increased from 11.2 nm (CS) to 101.7 nm (CSC). The surface texture is remarkably modified after C^{+5} and Ni^{+7} ions irradiation at the fluence of 1×10^{12} ions per square centimeter. As an impact of C^{+5} and Ni^{+7} MeV ions, the values of R_a examined to reduce 30.1 nm and 8.9 nm, respectively. The polymeric surface as shown in Figure 4.15(c and d) became ~70 % and ~91 % smoother upon carbon and nickel ions irradiation, respectively, that is, nickel ion exhibited nearly 21 % more impression. Hence, localized surface diffusion and hitting impact in the case of nickel ions is more pronounced than the other one. Briefly, the disruption of hillock structure owing to nickel ions is prevailing and developed a flatter surface more efficiently than carbon ions.

4.3 Conclusions

The flexible, self-sustained biodegradable SPE-based chitosan and silver salt was successfully prepared and exposed in a well-controlled environment with carbon and nickel ions of MeV energy at different fluences. The physicochemical and electrical characteristics of biodegradable SPE system are studied. The IR studies carried out to unfold the effects of the energetic ion on vital bond structure showed scissioning and structural degradation. Therefore the biodegradable SPE sample is *carbonized* and thus waning in E_g is perceived. Amendment in optical feature is state forwardly relevant to the ion-induced defects and/or structural deterioration. Accordingly, the frequency and fluence dependent behavior of the AC electrical properties is reasonably improved due to MeV ions irradiation. The investigation of imaginary electric modulus suggested non-Debye type of relaxation dynamics in the SPE matrices. The

chitosan-silver nitrate SPE system exhibited the hopping of charge carriers transport mechanism and conductivity follows the Jonscher universal power law. MeV ions impart a huge impact on values of R_a as examined from AFM studies. Meanwhile, distinctive studies relevance to the physicochemical perspective indicates that the nickel ions of heavier mass and superior S_e revealed more signature effects than the carbon ions of relatively lighter mass and moderate S_e . Pertinently, besides ion fluence, ion profile (i.e., mass, size, and energy) also play a crucial and versatile pioneer in enhancing the functional characteristics of the environment-friendly soft biodegradable system, which can be potentially used as electrolytes.

REFERENCES

- [1] J. Ma, Y. Sahai, Chitosan biopolymer for fuel cell applications, *Carbohydr. Polym.* 92 (2013) 955–975. doi:10.1016/j.carbpol.2012.10.015.
- [2] K. Sakurai, Glass transition temperature of chitosan and miscibility of chitosan/poly(N-vinyl pyrrolidone) blends, *Polymer (Guildf)*. 41 (2000) 7051–7056. doi:10.1016/S0032-3861(00)00067-7.
- [3] D. Enescu, C.E. Olteanu, Functionalized chitosan and its use in pharmaceutical, biomedical, and biotechnological research, *Chem. Eng. Commun.* 195 (2008) 1269–1291. doi:10.1080/00986440801958808.
- [4] S. Kumar-Krishnan, E. Prokhorov, M. Ramírez, M. a. Hernandez-Landaverde, D.G. Zarate-Triviño, Y. Kovalenko, I.C. Sanchez, J. Méndez-Nonell, G. Luna-Bárceñas, Novel gigahertz frequency dielectric relaxations in chitosan films, *Soft Matter*. 10 (2014) 8673–8684. doi:10.1039/C4SM01804D.
- [5] Y.N. Sudhakar, M. Selvakumar, D.K. Bhat, LiClO₄-doped plasticized chitosan and poly(ethylene glycol) blend as biodegradable polymer electrolyte for supercapacitors, *Ionics (Kiel)*. 19 (2013) 277–285. doi:10.1007/s11581-012-0745-5.
- [6] V.K. Sharma, R.A. Yngard, Y. Lin, Silver nanoparticles: Green synthesis and their antimicrobial activities, *Adv. Colloid Interface Sci.* 145 (2009) 83–96. doi:10.1016/j.cis.2008.09.002.
- [7] S. Kumar-Krishnan, E. Prokhorov, M. Hernández-Iturriaga, J.D. Mota-Morales, M. Vázquez-Lepe, Y. Kovalenko, I.C. Sanchez, G. Luna-Bárceñas, Chitosan/silver nanocomposites: Synergistic antibacterial action of silver nanoparticles and silver ions, *Eur. Polym. J.* 67 (2015) 242–251. doi:10.1016/j.eurpolymj.2015.03.066.
- [8] G. Hirankumar, S. Selvasekarapandian, M.S. Bhuvaneswari, R. Baskaran, M. Vijayakumar, Ag⁺ ion transport studies in a polyvinyl alcohol-based polymer electrolyte system, *J. Solid State Electrochem.* 10 (2006) 193–197. doi:10.1007/s10008-004-0612-z.
- [9] G. Hirankumar, S. Selvasekarapandian, M.S. Bhuvaneswari, R. Baskaran, M. Vijayakumar, Ag⁺ ion transport studies in a polyvinyl alcohol-based polymer electrolyte system, *J. Solid State Electrochem.* 10 (2006) 193–197. doi:10.1007/s10008-004-0612-z.
- [10] L. Vinet, A. Zhedanov, A ‘missing’ family of classical orthogonal polynomials, *J. Phys. A Math. Theor.* 44 (2011) 085201. doi:10.1088/1751-8113/44/8/085201.
- [11] J.R. Fried, *Polymer Science and Technology*, 3rd ed., Prentice Hall Press, USA, 2014.
- [12] S.B. Aziz, Z.H.Z. Abidin, A.K. Arof, Effect of silver nanoparticles on the DC conductivity in chitosan–silver triflate polymer electrolyte, *Phys. B Condens. Matter*. 405 (2010) 4429–4433. doi:10.1016/j.physb.2010.08.008.

- [13] S.B. Aziz, Z.H. Z. Abidin, A. K. Arof, Influence of silver ion reduction on electrical modulus parameters of solid polymer electrolyte based on chitosan-silver triflate electrolyte membrane, *Express Polym. Lett.* 4 (2010) 300–310. doi:10.3144/expresspolymlett.2010.38.
- [14] U. Kreibig, G. Bour, A. Hilger, M. Gartz, Optical Properties of Cluster–Matter: Influences of Interfaces, *Phys. Status Solidi.* 175 (1999) 351–366. doi:10.1002/(SICI)1521-396X(199909)175:1<351::AID-PSSA351>3.0.CO;2-U.
- [15] M.F. Zaki, Gamma-induced modification on optical band gap of CR-39 SSNTD, *J. Phys. D. Appl. Phys.* 41 (2008) 175404. doi:10.1088/0022-3727/41/17/175404.
- [16] V. Kumar, R.G. Sonkawade, S.K. Chakarvarti, P. Kulriya, K. Kant, N.L. Singh, A.S. Dhaliwal, Study of optical, structural and chemical properties of neutron irradiated PADC film, *Vacuum.* 86 (2011) 275–279. doi:10.1016/j.vacuum.2011.07.001.
- [17] J. Tauc, Optical properties and electronic structure of amorphous Ge and Si, *Mater. Res. Bull.* 3 (1968) 37–46. doi:10.1016/0025-5408(68)90023-8.
- [18] J. Robertson, E.P. O'Reilly, Electronic and atomic structure of amorphous carbon, *Phys. Rev. B.* 35 (1987) 2946–2957. doi:10.1103/PhysRevB.35.2946.
- [19] N. Vukmirović, L.-W. Wang, Density of States and Wave Function Localization in Disordered Conjugated Polymers: A Large Scale Computational Study, *J. Phys. Chem. B.* 115 (2011) 1792–1797. doi:10.1021/jp1114527.
- [20] G. Compagnini, G. Foti, R. Reitano, G. Mondio, Graphitic clusters in hydrogenated amorphous carbon induced by keV-ion irradiation, *Appl. Phys. Lett.* 57 (1990) 2546–2548. doi:10.1063/1.103832.
- [21] D. Fink, W.H. Chung, R. Klett, A. Schmoltdt, J. Cardoso, R. Montiel, M.H. Vazquez, L. Wang, F. Hosoi, H. Omichi, P. Goppelt-Langer, Carbonaceous clusters in irradiated polymers as revealed by UV-Vis spectrometry, *Radiat. Eff. Defects Solids.* 133 (1995) 193–208. doi:10.1080/10420159508223990.
- [22] D. Fink, R. Klett, L.T. Chadderton, J. Cardoso, R. Montiel, H. Vazquez, A. a. Karanovich, Carbonaceous clusters in irradiated polymers as revealed by small angle X-ray scattering and ESR, *Nucl. Instruments Methods Phys. Res. Sect. B Beam Interact. with Mater. Atoms.* 111 (1996) 303–314. doi:10.1016/0168-583X(95)01433-0.
- [23] N.L. Singh, A. Qureshi, F. Singh, D.K. Avasthi, Effect of swift heavy ion irradiation on dielectrics properties of polymer composite films, *Mater. Sci. Eng. B.* 137 (2007) 85–92. doi:10.1016/j.mseb.2006.10.013.
- [24] A.K. Jonscher, *Universal relaxation law: a sequel to Dielectric relaxation in solids*, Chelsea Dielectrics Press, 1996.
- [25] F. Kremer, A. Schönhals, *Broadband Dielectric Spectroscopy*, Springer Berlin Heidelberg, Berlin, Heidelberg, 2003. doi:10.1007/978-3-642-56120-7.

- [26] Y. Fu, K. Pathmanathan, J.R. Stevens, Dielectric and conductivity relaxation in poly(propylene glycol)–lithium triflate complexes, *J. Chem. Phys.* 94 (1991) 6323–6329. doi:10.1063/1.460420.
- [27] G. Williams, D.C. Watts, Non-symmetrical dielectric relaxation behaviour arising from a simple empirical decay function, *Trans. Faraday Soc.* 66 (1970) 80. doi:10.1039/tf9706600080.
- [28] R. Bergman, General susceptibility functions for relaxations in disordered systems, *J. Appl. Phys.* 88 (2000) 1356–1365. doi:10.1063/1.373824.
- [29] A.S. Bhatt, D.K. Bhat, M.S. Santosh, C. Tai, Chitosan/NiO nanocomposites: a potential new dielectric material, *J. Mater. Chem.* 21 (2011) 13490. doi:10.1039/c1jm12011e.
- [30] G.B. Patel, S. Bhavsar, N.L. Singh, F. Singh, P.K. Kulriya, SHI induced modification in structural, optical, dielectric and thermal properties of poly ethylene oxide films, *Nucl. Instruments Methods Phys. Res. Sect. B Beam Interact. with Mater. Atoms.* 379 (2016) 156–161. doi:10.1016/j.nimb.2016.04.018.
- [31] N.L. Singh, A. Sharma, D.K. Avasthi, V. Shrinet, Temperature and frequency dependent electrical properties of 50 MeV Li³⁺ ion irradiated polymeric blends, *Radiat. Eff. Defects Solids.* 160 (2005) 99–107. doi:10.1080/10420150500116649.